

# Generation of Forsteritic Olivine (Fo<sub>99.8</sub>) by Subsolvus Oxidation in Basaltic Flows

MADALYN S. BLONDES<sup>1\*</sup>, MARK T. BRANDON<sup>1</sup>,  
PETER W. REINERS<sup>2</sup>, F. ZEB PAGE<sup>3,4</sup> AND NORIKO T. KITA<sup>3</sup>

<sup>1</sup>DEPARTMENT OF GEOLOGY AND GEOPHYSICS, YALE UNIVERSITY, NEW HAVEN, CT 06520, USA

<sup>2</sup>DEPARTMENT OF GEOSCIENCES, UNIVERSITY OF ARIZONA, TUCSON, AZ 85721, USA

<sup>3</sup>WISC-SIMS, DEPARTMENT OF GEOLOGY AND GEOPHYSICS, UNIVERSITY OF WISCONSIN, MADISON, WI 53706, USA

<sup>4</sup>GEOLOGY DEPARTMENT, OBERLIN COLLEGE, OBERLIN, OH 44074, USA

RECEIVED MAY 2, 2010; ACCEPTED JANUARY 16, 2012  
ADVANCE ACCESS PUBLICATION FEBRUARY 28, 2012

*We identify olivine grains with compositions up to Fo<sub>99.8</sub>, which are found in multiple primitive basaltic lava flows from a monogenetic volcano in the Big Pine Volcanic Field, California, USA. In this study, we show that the forsterite in these basalts formed by subsolvus recrystallization in a high-fO<sub>2</sub> environment. Olivine compositions are bimodal, with flows having either all normal compositions (Fo<sub>74.9–94.4</sub>) or highly forsteritic (Fo<sub>97.2–99.8</sub>) compositions. In many grains, the subhedral forsteritic olivine has a hematite and clinopyroxene rim, and internal parallel-oriented planes of hematite, clinopyroxene and orthopyroxene. Results of isotopic, chemical, crystallographic, petrographic and mineralogical analyses show that the forsterite formed through subsolvus oxidation of olivine phenocrysts. The forsteritic olivines generally occur in the thinner flows. We infer that a rapidly emplaced sequence of thin, vesicular, spatter-fed flows allowed the original olivine phenocrysts to become repeatedly reheated while exposed to air. Our study required sampling each flow, so it was difficult to avoid the altered portions of the thinner flows. Other studies would tend to avoid such flows, which may account for why such forsteritic olivines have not been more widely recognized.*

KEY WORDS: *forsterite; olivine; subsolvus oxidation, symplectite; vesicular basalt*

## INTRODUCTION

Olivine [(Mg,Fe)<sub>2</sub>SiO<sub>4</sub>] is the dominant mineral in the upper mantle and a common phenocryst in basalt. The

composition of olivine in peridotitic rocks is typically Fo<sub>86–91</sub>, whereas basaltic and komatiitic magmas crystallize olivine with a typical range of Fo<sub>85–96</sub> (Deer *et al.*, 1992). Published olivine compositions are rarely more magnesian than these ranges. For example, none of the nearly 17 000 olivine phenocrysts tabulated from basaltic rocks has a forsterite composition above Fo<sub>95</sub> (Sobolev *et al.*, 2007). However, rare occurrences of forsterite-rich olivine have been encountered in basalts or gabbros (Sigurdsson & Brown, 1970; Johnston & Stout, 1984a; Garcia *et al.*, 2000; Cortés *et al.*, 2006). Such forsterite olivine cannot be the product of equilibrium crystallization at oxygen fugacities [between quartz–fayalite–magnetite (QFM) and nickel–nickel oxide (NNO)] typical for mantle-derived basalts. To crystallize nearly forsteritic olivine of Fo<sub>95</sub> would require a high-magnesium melt with Mg-number ~0.85 (Roeder & Emslie, 1970), which is well above the value for any basalt or komatiite. Here we describe olivine phenocrysts from multiple primitive basalt flows from a monogenetic vent in the Big Pine Volcanic Field, California, USA that are the most forsteritic (up to Fo<sub>99.8</sub>) ever reported. For convenience, we refer to all olivine >Fo<sub>95</sub> as ‘forsterite’ and all olivine <Fo<sub>95</sub> as ‘olivine’. We present chemical, structural, and petrographic data to constrain the origin of these rare forsterite grains.

Rare end-member forsterite may form in a number of ways. At time-scales orders of magnitude too great to be applicable to lavas, meteoritic olivine exsolves at low

\*Corresponding author. Present address: US Geological Survey, Reston, VA 20192, USA. Telephone: 703-648-6509. E-mail: mblondes@usgs.gov

© The Author 2012. Published by Oxford University Press. All rights reserved. For Permissions, please e-mail: journals.permissions@oup.com

temperatures into forsteritic and fayalitic components (Petaev & Brearley, 1994). Forsterite  $>Fo_{95}$  has been recognized in ultramafic xenoliths or kimberlite nodules (Boyd & Nixon, 1978; Johnston & Stout, 1984a) and as olivine inclusions within diamonds (Sobolev *et al.*, 1970). It is also found as regenerated olivine in serpentinite bodies that have dehydrated in contact aureole or alpine peridotite settings (Vance & Dungan, 1977; Nozaka, 2003). Metamorphism of dolomite and limestone has been shown to produce high-Mg olivine, which is often found in partially assimilated carbonate xenoliths and carbonate contact aureoles (Trommsdorff & Evans, 1977; Ferry, 1994; Cook & Bowman, 2000; Owens, 2000; Wenzel *et al.*, 2002). Forsterite also may form under unusually oxidizing conditions, either syn- or post-crystallization. For example, Sigurdsson & Brown (1970) and Cortés *et al.* (2006) have argued that similar forsterite in basalts is the result of large-scale changes to the oxidation state of the magma, induced by transient degassing or the dissociation of water. Subsolidus oxidation of olivine converts  $Fe^{2+}$  in the octahedral site into  $Fe^{3+}$ . This cation no longer fits into the octahedral site and thus tends to precipitate in defect-rich parts of the olivine structure, such as dislocations (Kohlstedt & Vander Sande, 1975; Karato, 1987; Ando *et al.*, 2001). When held for long durations at high temperatures, pressures, and  $fO_2$ , the olivine will react to form  $Fe^{3+}$ -bearing magnetite or hematite and Si-rich enstatite or  $SiO_2$  (Haggerty & Baker, 1967; Champness, 1970; Goode, 1974; Nitsan, 1974; Kohlstedt & Vander Sande, 1975; Putnis, 1979; Johnston & Stout, 1984b; Banfield *et al.*, 1990; Ashworth & Chambers, 2000). This oxidation reaction forms a regular pattern of oxide and pyroxene symplectites within the host olivine (e.g. Ashworth & Chambers, 2000).

We investigated the origin of the Big Pine forsterite using structural, mineralogical, isotopic, and chemical data. First, we checked for a topotaxial relationship between the olivine and its internal phases. A topotaxial relationship [conversion from one mineral to one or more minerals with retained crystallographic orientation (Shannon & Rossi, 1964)] between a host olivine and its internal phases occurs only in magmatic settings or as a result of alteration of pre-existing minerals, commonly during oxidation. Second, we created electron microprobe element maps to determine the composition of the forsterite and its internal phases to see if the combined bulk composition equates to a normal phenocrystic olivine or a potential xenocrystic phase. Third, we measured the forsterite oxygen isotope composition to see if it is different from mid-ocean ridge basalt (MORB)-source olivine compositions ( $5.2 \pm 0.2\%$ ; Eiler *et al.*, 1997a; Eiler, 2001). Fourth, we explored any correlations between the bulk-rock composition and its included olivines that would suggest assimilation of xenolithic material.

## REGIONAL SETTING AND SAMPLES

The forsterite grains, which are the focus of this study, occur in basaltic lavas of the Big Pine Volcanic Field, a region of disperse monogenetic vents in Owens Valley, California, east of the Sierra Nevada and on the western edge of the Western Great Basin and Range province (Fig. 1). The origin of the Big Pine magmatism has been variously attributed to Basin-and-Range extension (e.g. Menzies *et al.*, 1983; Beard & Glazner, 1995), or to convective removal of lithospheric mantle beneath the southern Sierra Nevada (Ducea & Saleeby, 1998; Lee *et al.*, 2001; Zandt *et al.*, 2004). The Big Pine Volcanic Field is a set of one silicic and  $\sim 24$  basaltic monogenetic cinder cones with lava flows covering  $\sim 500 \text{ km}^2$ , ranging in age from 1.2 Ma to 30 ka (Blondes *et al.*, 2007, 2008, and references therein). The Papoose Canyon eruption, in which the forsterite is found, is composed of  $\sim 50$  stacked lava units that erupted over a  $10^0$ – $10^2$  year time-scale at  $755 \pm 41.5$  ka (Blondes *et al.*, 2008). The flows generally decrease in thickness throughout the sequence, with massive basalt flows up to 30 m thick in the lower part of the sequence, and spatter-fed vesicular flows only a few centimeters thick in the upper part (Fig. 1). Xenoliths, including peridotite, pyroxenite, and minor amounts of sedimentary and carbonate material, are present in the lower half of the sequence, but are rare in the upper half. The flows have well-defined compositional trends that covary closely with stratigraphic position (Blondes *et al.*, 2008).

## ANALYTICAL METHODS

All samples were studied in thin section under a petrographic microscope to determine their mineralogy and textural relationships. Mineral compositions, element maps and cathodoluminescence images were obtained using the Yale JEOL JXA-8600 electron microprobe. Chemical analyses were measured using quantitative wavelength-dispersive spectroscopy (WDS) with a 15 kV accelerating voltage, 15 nA current, and a focused beam. Element maps were generated by rastering the beam for at least 20 min for each image.

Relative orientation measurements of the host forsterite crystals and the internal oxides in sample 03MB43 were determined using the electron backscatter diffraction technique (EBSD) (Prior *et al.*, 1999) on the Yale FEI XL-30 ESEM-FEG scanning electron microscope. Crystal orientations for three olivine and nine hematite locations were determined using Channel 5+ software by HKL technology at 20 kV, 2.4 nA, and a working distance of 20 mm.

Four  $10 \mu\text{m}$  spots on the 03MB43 forsterite (Fig. 2a) were analyzed *in situ* for  $\delta^{18}\text{O}$  using the CAMECA 1280 ion microprobe at the Wisc-SIMS laboratory, University of Wisconsin, Madison. The analyzed grain was within

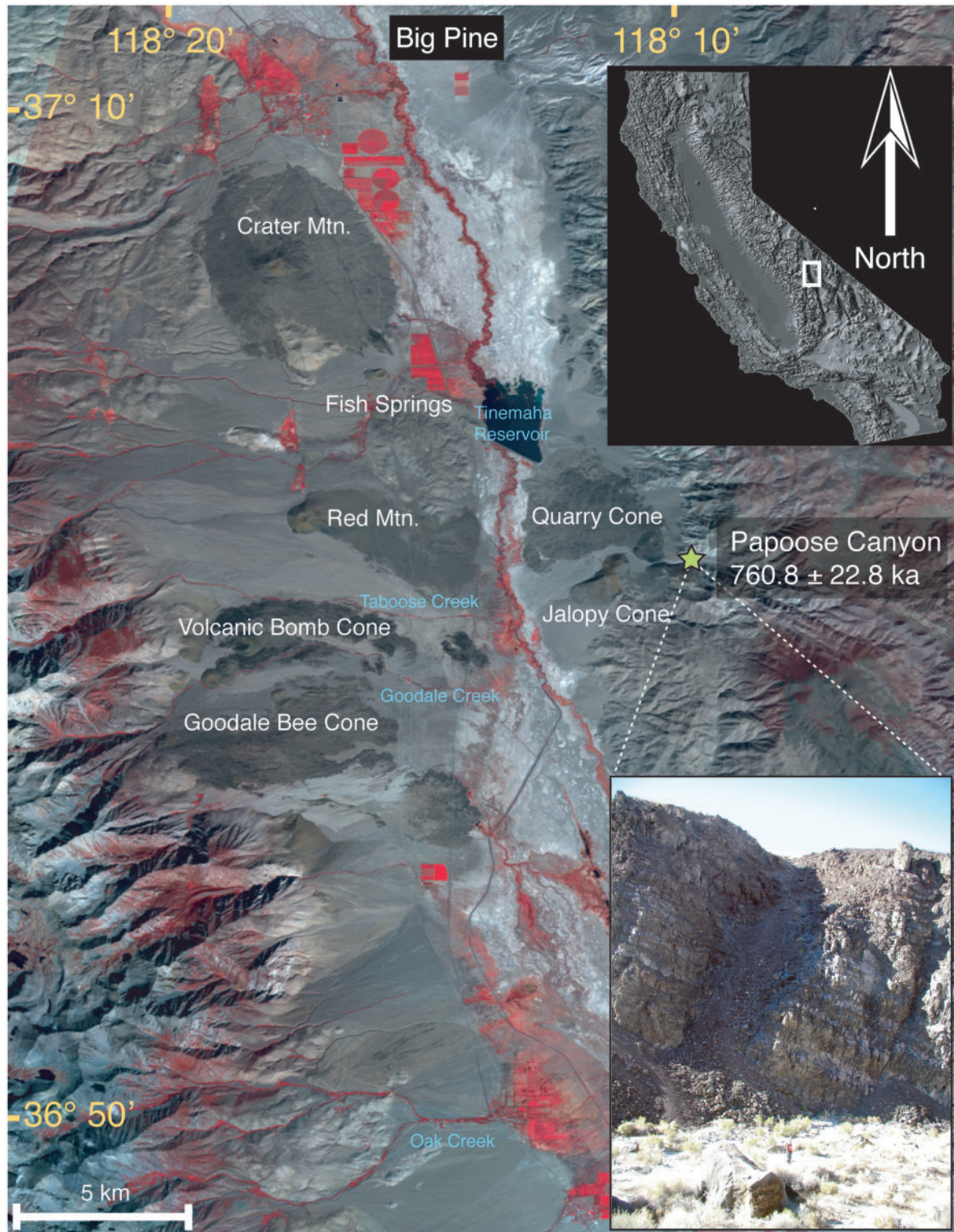


**Fig. 1.** Map of the Big Pine Volcanic Field. Adapted from Blondes *et al.* (2008). The lower inset shows the later half of the Papoose Canyon single eruption sequence where the forsterite is found. The author is for scale at the bottom of the image.

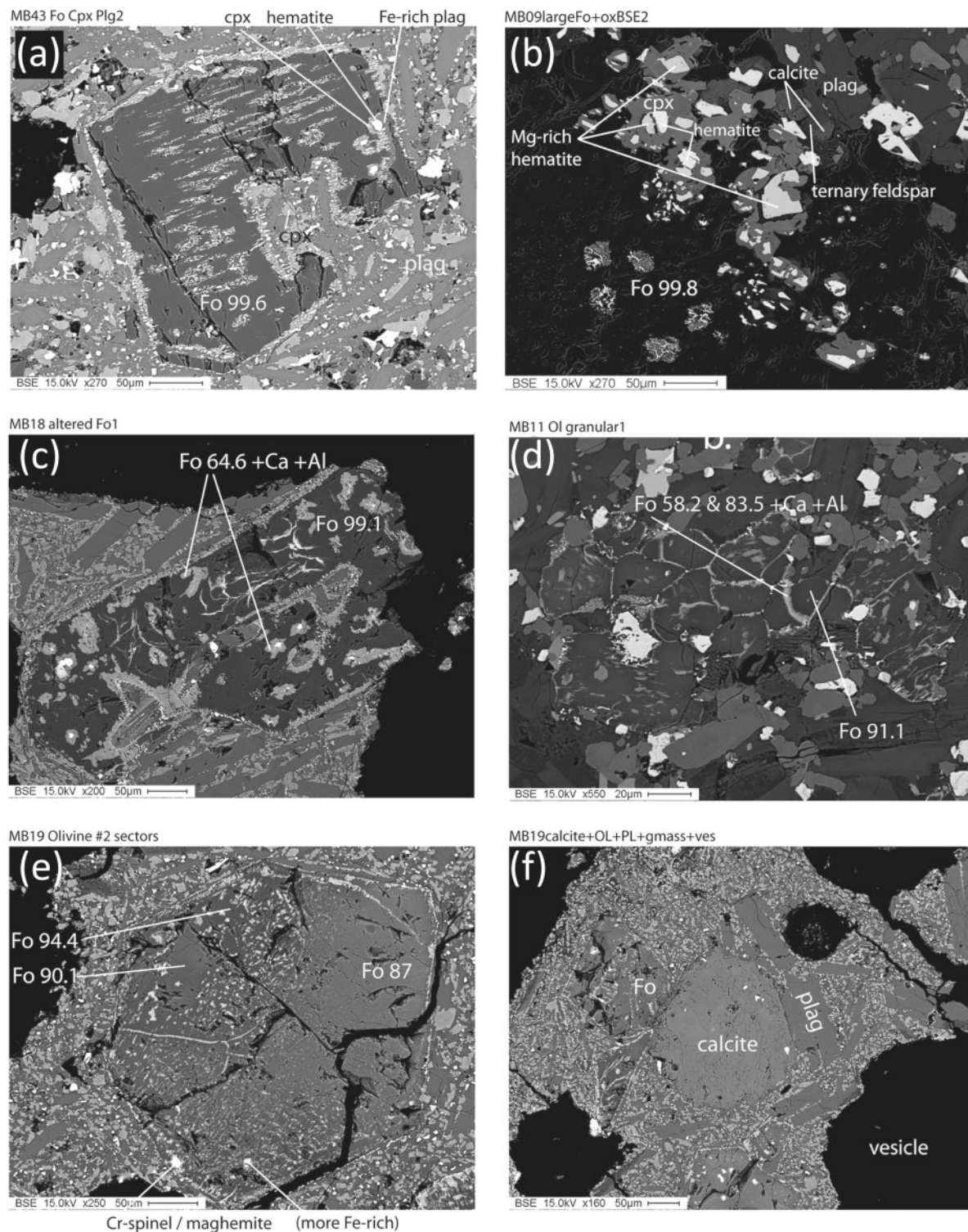


**Fig. 2.** Olivine phases and textures in the Papoose Canyon single eruption sequence. Images are backscatter electron (BSE) images at a range of scales. The older flows (03MB43) are at the top left of the image and the younger flows (03MB19) are at the bottom. (a) 03MB43 olivine grain (03MB43 $\otimes$ ) with subparallel planes of hematite and cpx within the forsterite host. Two Fe-rich plagioclase crystals are also found along cracks within the olivine. (b) (03MB09) and (c) (03MB18) show other forsterite grains and one region with calcite next to a vesicle. (b) (03MB09) shows the olivine with the highest forsterite content of  $Fo_{99.8}$ . Symplectites of hematite and cpx can be seen in the lower left of the image. (d) (03MB11) sample with normal olivine. There are small 'splotches' and 'wisps' of a material with an olivine composition with high concentrations of Al and Ca. This may be true olivine, multiphase material, or too small to determine a reliable composition with a focused beam. (e) (03MB19) contains an olivine crystal that ranges in composition from  $Fo_{87}$  to  $Fo_{94.4}$ . Where there is less Fe in the olivine the Fe-oxides are larger. (f) (03MB19) calcite within a vesicle adjacent to a forsterite crystal.

5 mm of the center of a 2.54 mm round thin section. A grain of San Carlos olivine standard (Fo<sub>89</sub>, Kita *et al.*, 2009) was mounted adjacent to the sample grain and the section was polished so that the sample and standard were coplanar. Instrument parameters were similar to those reported by Kita *et al.* (2009) to achieve high secondary ion transmission. The intensity of <sup>16</sup>O was (2–3) × 10<sup>9</sup> c.p.s. depending on the primary intensity (*c.* 10<sup>9</sup> c.p.s. nA<sup>-1</sup>). Mass resolving power (MRP, M/ΔM), measured at 10% peak height, was set to *c.* 2200, enough to separate hydride interferences on <sup>18</sup>O. Two Faraday cups (FC) were used to measure <sup>16</sup>O and <sup>18</sup>O simultaneously and the amplifiers on each were equipped with 10<sup>10</sup> and 10<sup>11</sup> Ω resistors, respectively. The base line of the FC amplifiers was measured at the beginning of each analytical session; drift during the day was insignificant compared with the noise level of the detectors (≤1000 c.p.s. for the <sup>18</sup>O FC with 10<sup>11</sup> Ω resistor; Kita *et al.*, 2009). At each analysis position, any small misalignment of the secondary optics owing to changing stage position was automatically retuned before analysis. The four sample analyses were bracketed by eight analyses of the San Carlos olivine standard, the reproducibility of which yielded a spot-to-spot uncertainty of 0.43‰ (see Supplementary Data Electronic Appendix), which is taken as the 2σ analytical uncertainty. Analysis of oxygen isotopes by ion microprobe can be complicated by a matrix effect that introduces a systematic bias owing to differing cation compositions in sample and standard (e.g. Eiler *et al.*, 1997*b*; Page *et al.*, 2010). We compared the instrumental bias between the San Carlos standard (Fo<sub>89</sub>) and a synthetic pure forsterite standard and found it to differ by less than 0.1‰. Because this difference was small relative to the analytical uncertainty, no further bias correction was applied.

## RESULTS

We determined mineral compositions for 11 samples from the Papoose Canyon sequence. These represent a subset of the 25 samples reported by Blondes *et al.* (2008) in which whole-rock major and trace element data are reported. For the microprobe analyses, four of the samples had only forsteritic olivine (>Fo<sub>99</sub>, Table 1), whereas the remaining seven samples had only normal olivine (<Fo<sub>95</sub>).

All of the forsterite-bearing samples have a vesicular groundmass, which is typically red in color. The forsterites contain many inclusions, so much so that they are locally black in color. The inclusions are, in order of decreasing abundance: hematite, clinopyroxene, orthopyroxene, chromite, and plagioclase (Fig. 2). Symplectites of pyroxene and oxides are present in samples 03MB09 and 03MB43 (Fig. 2a and b). From a view off-normal to the symplectite plane, their thin, laminar textures are evident (Fig. 2a). Microbeam analysis indicates that the internal symplectites consist of hematite, clinopyroxene, and orthopyroxene, and the forsterite rim contains non-preferentially

oriented clinopyroxene and hematite (Figs 2a and 3, Table 2). In addition to the dominant plagioclase in the basalt groundmass, phases in contact but external to the forsterite include plagioclase, alkali feldspar, calcite, pyroxenes, hematite, and magnetite (Fig. 2b). Other forsterite-bearing samples have wispy or granular textures with no symplectite or apparent oriented structure (Fig. 2c and d). Olivine in 03MB11 and 03MB18 has a more Fe-rich composition ranging from Fo<sub>58</sub> to Fo<sub>65</sub>, but this may be an artifact owing to overlapping of the beam with adjacent minerals (Fig. 2c and d). Fe-rich domains are found between equant oxides and the surrounding forsterite (Fig. 2c) or cutting through olivine crystals (Fig. 2d). There is abundant hematite, commonly with small concentrations of other cations including Cr, Ti, and Mg. In one thin section, a small region 150 μm across contains, in decreasing order of abundance, forsterite (Fo<sub>99-8</sub>), hematite, magnesioferrite, clinopyroxene, calcite, plagioclase, and a ternary feldspar (Fig. 2b). Some samples lacking forsterite contain similar wispy and granular fayalitic components, but lack any hematite in the olivine or groundmass (Fig. 2d and e).

Four δ<sup>18</sup>O analyses within one forsterite (03MB43⊗) have typical mantle-like olivine values of 5.4 ± 0.3‰ (1σ, 10 μm spots) (Table 3; Supplementary Data Electronic Appendix). EBSD results show that all Fe-oxide phases [determined to be either Fe<sub>2</sub>O<sub>3</sub> or Fe<sub>3</sub>O<sub>4</sub> from electron microprobe analysis (EMPA)] in the 03MB43⊗ grain are trigonal hematite, rather than cubic maghemite. The [100] direction of olivine is parallel to the [0001] direction of hematite, indicating a topotaxial relationship between olivine and the internal hematite (Fig. 3). No such topotaxial relationship exists for the pyroxenes.

## DISCUSSION

### Xenocrystic assimilation

There exists the possibility that the forsterites are xenocrysts derived from local lithologies with forsteritic olivine such as carbonates or dehydrated serpentinites. The southern Sierra Nevada and the transition to the Basin and Range Province contain ophiolites (Saleeby, 1982), dolomitic skarns (Shieh & Taylor, 1969), and a hydrated mantle wedge that one would expect to be present beneath the Sierran magmatic arc. Forsterite is highly refractory with a melting temperature of 1890°C at 1 atm, and thus would be able to survive as a xenocryst in a magma (Bowen & Schairer, 1935). The isotopic and chemical data, however, show that assimilation of carbonates or dehydrated serpentinites is highly unlikely.

Carbonates generally have heavy δ<sup>18</sup>O (20–30‰) at low temperatures (200–500°C; Valley, 1986) relative to normal xenolithic MORB-source upper mantle olivine (5.2 ± 0.2‰) (Eiler *et al.*, 1997*a*; Eiler, 2001). In the nearby Birch Creek forsteritic marble, calcite, dolomite, and forsterite have a δ<sup>18</sup>O range of 20.5–24.2‰ (Shieh & Taylor,

Table 1: Olivine compositions

Sample	n	Results in oxide wt %									Cations based on 4 oxygens										
		SiO <sub>2</sub>	TiO <sub>2</sub>	Al <sub>2</sub> O <sub>3</sub>	Cr <sub>2</sub> O <sub>3</sub>	MgO	CaO	MnO	FeO	NiO	Sum	Si	Ti	Al	Cr	Mg	Ca	Mn	Fe	Ni	Fo
03MB29 C	36	39.5	0.07	0.08	0.00	45.2	0.24	0.14	15.2	0.21	100.7	0.99	0.00	0.00	0.00	1.69	0.01	0.00	0.32	0.00	84.1
03MB29 C	37	39.4	0.00	0.07	0.00	43.3	0.18	0.25	16.8	0.22	100.1	1.00	0.00	0.00	0.00	1.63	0.01	0.01	0.36	0.01	82.1
03MB29 C	38	40.0	0.00	0.03	0.01	44.4	0.29	0.24	15.4	0.16	100.6	1.00	0.00	0.00	0.00	1.66	0.01	0.01	0.32	0.00	83.7
03MB29 C	39	39.5	0.45	0.05	0.04	45.5	0.60	0.12	14.0	0.21	100.5	0.99	0.01	0.00	0.00	1.69	0.02	0.00	0.29	0.00	85.3
03MB29 C	40	39.6	0.54	0.08	0.02	46.0	0.00	0.22	13.7	0.20	100.4	0.99	0.01	0.00	0.00	1.71	0.00	0.01	0.29	0.00	85.7
03MB29 R	42	39.1	0.05	0.03	0.00	40.2	0.30	0.41	20.6	0.12	100.8	1.00	0.00	0.00	0.00	1.54	0.01	0.01	0.44	0.00	77.7
03MB29 R	43	38.7	0.02	0.05	0.00	39.7	0.34	0.51	21.3	0.11	100.7	1.00	0.00	0.00	0.00	1.53	0.01	0.01	0.46	0.00	76.9
03MB29 R	44	38.6	0.00	0.02	0.00	38.9	0.31	0.48	21.9	0.07	100.4	1.00	0.00	0.00	0.00	1.50	0.01	0.01	0.48	0.00	76.0
03MB29 R	45	38.6	0.06	0.04	0.00	38.5	0.35	0.45	23.0	0.12	101.1	1.00	0.00	0.00	0.00	1.48	0.01	0.01	0.50	0.00	74.9
03MB29 gr	46	38.1	0.01	0.01	0.00	37.7	0.35	0.53	22.8	0.09	99.6	1.00	0.00	0.00	0.00	1.48	0.01	0.01	0.50	0.00	74.7
03MB30 C	137	40.9	0.02	0.07	0.06	47.8	0.24	0.16	11.7	0.29	101.2	1.00	0.00	0.00	0.00	1.74	0.01	0.00	0.24	0.01	87.9
03MB30 C	138	39.9	0.02	0.05	0.02	46.2	0.20	0.25	13.1	0.24	100.0	1.00	0.00	0.00	0.00	1.72	0.01	0.01	0.27	0.01	86.2
03MB30 C	139	40.0	0.01	0.07	0.00	46.7	0.20	0.23	12.8	0.26	100.2	0.99	0.00	0.00	0.00	1.73	0.01	0.01	0.27	0.01	86.7
03MB30 C	140	40.0	0.07	0.09	0.04	44.8	0.24	0.22	14.4	0.15	100.0	1.00	0.00	0.00	0.00	1.67	0.01	0.01	0.30	0.00	84.7
03MB30 C	141	40.4	0.00	0.05	0.00	46.7	0.20	0.14	12.7	0.23	100.3	1.00	0.00	0.00	0.00	1.73	0.01	0.00	0.26	0.01	86.8
03MB30 R	142	39.4	0.05	0.04	0.00	43.6	0.37	0.26	15.7	0.16	99.5	1.00	0.00	0.00	0.00	1.65	0.01	0.01	0.33	0.00	83.2
03MB30 R	143	39.7	0.07	0.08	0.02	42.3	0.37	0.28	17.6	0.16	100.6	1.00	0.00	0.00	0.00	1.60	0.01	0.01	0.37	0.00	81.0
03MB30 R	145	38.7	0.05	0.07	0.00	42.0	0.44	0.30	17.9	0.15	99.6	0.99	0.00	0.00	0.00	1.61	0.01	0.01	0.38	0.00	80.7
03MB30 R	146	39.2	0.03	0.05	0.00	44.0	0.33	0.23	15.4	0.19	99.4	1.00	0.00	0.00	0.00	1.66	0.01	0.01	0.33	0.00	83.6
03MB37 C	81	38.7	0.21	0.03	0.00	39.1	0.07	0.52	21.6	0.08	100.2	1.00	0.00	0.00	0.00	1.51	0.00	0.01	0.47	0.00	76.4
03MB37 C	82	39.1	0.09	0.03	0.00	39.4	0.27	0.48	20.8	0.09	100.1	1.01	0.00	0.00	0.00	1.51	0.01	0.01	0.45	0.00	77.1
03MB37 C	83	38.7	0.02	0.03	0.00	39.2	0.34	0.46	21.7	0.11	100.6	1.00	0.00	0.00	0.00	1.51	0.01	0.01	0.47	0.00	76.3
03MB37 C	84	40.1	0.07	0.04	0.03	46.9	0.07	0.16	13.1	0.27	100.7	0.99	0.00	0.00	0.00	1.73	0.00	0.00	0.27	0.01	86.5
03MB37 C	85	40.5	0.03	0.05	0.01	46.0	0.31	0.13	13.0	0.16	100.1	1.01	0.00	0.00	0.00	1.70	0.01	0.00	0.27	0.00	86.4
03MB37 R	86	38.6	0.07	0.02	0.00	38.9	0.27	0.47	21.1	0.12	99.5	1.00	0.00	0.00	0.00	1.51	0.01	0.01	0.46	0.00	76.7
03MB37 R	87	38.6	0.06	0.04	0.00	39.0	0.28	0.45	21.3	0.12	99.8	1.00	0.00	0.00	0.00	1.51	0.01	0.01	0.46	0.00	76.5
03MB37 R	88	38.7	0.24	0.04	0.00	39.1	0.26	0.61	21.2	0.11	100.3	1.00	0.01	0.00	0.00	1.51	0.01	0.01	0.46	0.00	76.6
03MB37 R	89	38.8	0.00	0.04	0.00	39.1	0.44	0.39	20.3	0.14	99.1	1.01	0.00	0.00	0.00	1.52	0.01	0.01	0.44	0.00	77.5
03MB37 R	90	39.2	0.06	0.11	0.00	39.0	0.31	0.56	20.7	0.07	100.0	1.01	0.00	0.00	0.00	1.50	0.01	0.01	0.45	0.00	77.0
03MB37 ba	91	38.9	0.00	0.02	0.00	39.0	0.26	0.47	21.9	0.14	100.7	1.00	0.00	0.00	0.00	1.50	0.01	0.01	0.47	0.00	76.0
03MB40 C	192	38.3	0.03	0.02	0.00	38.9	0.12	0.44	20.5	0.16	98.4	1.00	0.00	0.00	0.00	1.52	0.00	0.01	0.45	0.00	77.2
03MB40 C	193	38.5	0.01	0.02	0.00	39.8	0.20	0.51	20.8	0.11	99.8	1.00	0.00	0.00	0.00	1.54	0.01	0.01	0.45	0.00	77.3
03MB40 C	194	38.1	0.07	0.03	0.00	38.6	0.23	0.53	21.0	0.10	98.7	1.00	0.00	0.00	0.00	1.51	0.01	0.01	0.46	0.00	76.6
03MB40 C	195	37.6	0.02	0.06	0.01	38.8	0.23	0.41	21.0	0.10	98.3	0.99	0.00	0.00	0.00	1.53	0.01	0.01	0.46	0.00	76.7
03MB40 C	196	37.9	0.04	0.06	0.04	38.5	0.21	0.50	21.6	0.14	99.1	1.00	0.00	0.00	0.00	1.51	0.01	0.01	0.48	0.00	76.1
03MB40 R	197	37.6	0.06	0.05	0.01	37.6	0.24	0.58	22.2	0.07	98.4	1.00	0.00	0.00	0.00	1.49	0.01	0.01	0.49	0.00	75.1
03MB40 R	198	37.8	0.07	0.02	0.00	39.5	0.23	0.49	20.3	0.06	98.4	0.99	0.00	0.00	0.00	1.55	0.01	0.01	0.45	0.00	77.6
03MB40 R	200	37.7	0.05	0.06	0.00	38.3	0.22	0.53	21.0	0.09	98.0	1.00	0.00	0.00	0.00	1.51	0.01	0.01	0.47	0.00	76.4
03MB40 R	201	38.4	0.05	0.02	0.01	39.3	0.25	0.54	21.2	0.14	100.0	1.00	0.00	0.00	0.00	1.52	0.01	0.01	0.46	0.00	76.7
03MB43 C	47	43.0	0.07	0.05	0.00	57.7	0.10	0.40	0.43	0.14	101.9	0.99	0.00	0.00	0.00	1.99	0.00	0.01	0.01	0.00	99.6
03MB43 C	48	42.5	0.07	0.03	0.00	57.3	0.09	0.35	0.56	0.21	101.1	0.99	0.00	0.00	0.00	1.99	0.00	0.01	0.01	0.00	99.5
03MB43 C	49	42.7	0.02	0.01	0.00	57.5	0.03	0.37	0.65	0.21	101.5	0.99	0.00	0.00	0.00	1.99	0.00	0.01	0.01	0.00	99.4
03MB43 C	50	42.9	0.00	0.03	0.00	57.1	0.05	0.37	0.58	0.22	101.3	1.00	0.00	0.00	0.00	1.98	0.00	0.01	0.01	0.00	99.4
03MB43 C	51	42.6	0.00	0.02	0.00	57.2	0.03	0.32	0.72	0.22	101.1	0.99	0.00	0.00	0.00	1.99	0.00	0.01	0.01	0.00	99.3

(continued)

Table 1: Continued

Sample	n	Results in oxide wt %										Cations based on 4 oxygens									
		SiO <sub>2</sub>	TiO <sub>2</sub>	Al <sub>2</sub> O <sub>3</sub>	Cr <sub>2</sub> O <sub>3</sub>	MgO	CaO	MnO	FeO	NiO	Sum	Si	Ti	Al	Cr	Mg	Ca	Mn	Fe	Ni	Fo
03MB43 R	52	42.8	0.10	0.03	0.00	57.5	0.16	0.42	0.51	0.16	101.6	0.99	0.00	0.00	0.00	1.99	0.00	0.01	0.01	0.00	99.5
03MB43 R	53	42.7	0.02	0.05	0.00	57.3	0.13	0.49	0.35	0.14	101.2	0.99	0.00	0.00	0.00	1.99	0.00	0.01	0.01	0.00	99.7
03MB43 R	54	42.7	0.06	0.06	0.01	57.3	0.10	0.35	0.62	0.18	101.4	0.99	0.00	0.00	0.00	1.98	0.00	0.01	0.01	0.00	99.4
03MB43 R	55	42.4	0.00	0.03	0.01	57.6	0.12	0.33	0.56	0.19	101.2	0.99	0.00	0.00	0.00	2.00	0.00	0.01	0.01	0.00	99.5
03MB43 R	56	42.4	0.03	0.03	0.00	57.7	0.11	0.34	0.71	0.19	101.6	0.99	0.00	0.00	0.00	2.00	0.00	0.01	0.01	0.00	99.3
03MB07 C	183	37.0	0.03	0.02	0.00	36.6	0.15	0.52	23.9	0.07	98.2	0.99	0.00	0.00	0.00	1.46	0.00	0.01	0.54	0.00	73.2
03MB07 C	184	37.2	0.07	0.01	0.01	36.9	0.24	0.50	23.5	0.12	98.5	0.99	0.00	0.00	0.00	1.47	0.01	0.01	0.52	0.00	73.7
03MB07 C	186	36.8	0.05	0.05	0.01	37.0	0.30	0.52	23.4	0.12	98.2	0.99	0.00	0.00	0.00	1.48	0.01	0.01	0.53	0.00	73.8
03MB07 R	187	36.8	0.05	0.03	0.00	36.2	0.26	0.56	24.6	0.12	98.6	0.99	0.00	0.00	0.00	1.45	0.01	0.01	0.55	0.00	72.5
03MB07 R	188	36.5	0.04	0.02	0.00	36.3	0.25	0.59	24.2	0.08	98.1	0.99	0.00	0.00	0.00	1.46	0.01	0.01	0.55	0.00	72.8
03MB07 R	190	37.1	0.07	0.01	0.00	36.3	0.22	0.54	23.8	0.10	98.0	1.00	0.00	0.00	0.00	1.45	0.01	0.01	0.53	0.00	73.1
03MB09 C	202	42.2	0.05	0.01	0.00	56.1	0.16	0.46	0.38	0.14	99.5	1.00	0.00	0.00	0.00	1.98	0.00	0.01	0.01	0.00	99.6
03MB09 C	203	41.7	0.03	0.03	0.00	56.2	0.11	0.40	0.37	0.15	99.0	0.99	0.00	0.00	0.00	1.99	0.00	0.01	0.01	0.00	99.6
03MB09 C	204	41.8	0.00	0.04	0.00	55.9	0.15	0.28	0.32	0.09	98.5	1.00	0.00	0.00	0.00	1.99	0.00	0.01	0.01	0.00	99.7
03MB09 C	205	41.5	0.00	0.02	0.00	56.0	0.12	0.40	0.46	0.20	98.7	0.99	0.00	0.00	0.00	1.99	0.00	0.01	0.01	0.00	99.5
03MB09 C	206	41.9	0.00	0.06	0.00	56.6	0.12	0.37	0.34	0.11	99.4	0.99	0.00	0.00	0.00	2.00	0.00	0.01	0.01	0.00	99.7
03MB09 R	207	41.8	0.03	0.05	0.00	56.3	0.10	0.46	0.45	0.07	99.3	0.99	0.00	0.00	0.00	1.99	0.00	0.01	0.01	0.00	99.6
03MB09 R	210	41.8	0.03	0.03	0.00	55.7	0.22	0.41	0.33	0.12	98.7	1.00	0.00	0.00	0.00	1.98	0.01	0.01	0.01	0.00	99.7
03MB09 R	211	42.1	0.04	0.07	0.00	56.7	0.07	0.32	0.20	0.10	99.6	0.99	0.00	0.00	0.00	2.00	0.00	0.01	0.00	0.00	99.8
03MB11 C	108	39.9	0.02	0.05	0.00	44.9	0.23	0.27	14.8	0.20	100.4	1.00	0.00	0.00	0.00	1.67	0.01	0.01	0.31	0.00	84.4
03MB11 C	109	38.7	0.02	0.06	0.00	40.2	0.23	0.46	20.9	0.16	100.8	0.99	0.00	0.00	0.00	1.54	0.01	0.01	0.45	0.00	77.4
03MB11 C	110	39.5	0.03	0.03	0.01	44.3	0.14	0.24	16.5	0.06	100.9	0.99	0.00	0.00	0.00	1.66	0.00	0.01	0.35	0.00	82.7
03MB11 C	111	40.0	0.00	0.06	0.03	44.9	0.19	0.26	15.1	0.22	100.7	1.00	0.00	0.00	0.00	1.67	0.01	0.01	0.32	0.00	84.1
03MB11 C	112	39.9	0.02	0.03	0.00	46.4	0.09	0.12	13.2	0.24	100.1	1.00	0.00	0.00	0.00	1.72	0.00	0.00	0.28	0.01	86.2
03MB11 R	113	38.7	0.05	0.03	0.01	38.5	0.25	0.56	22.2	0.08	100.3	1.00	0.00	0.00	0.00	1.49	0.01	0.01	0.48	0.00	75.5
03MB11 R	114	38.3	0.08	0.02	0.00	38.6	0.26	0.58	22.5	0.13	100.5	1.00	0.00	0.00	0.00	1.50	0.01	0.01	0.49	0.00	75.3
03MB11 R	115	38.3	0.03	0.03	0.02	38.4	0.18	0.57	22.2	0.09	99.9	1.00	0.00	0.00	0.00	1.49	0.01	0.01	0.48	0.00	75.5
03MB11 R	116	39.1	0.03	0.05	0.03	41.9	0.26	0.38	17.5	0.16	99.3	1.00	0.00	0.00	0.00	1.60	0.01	0.01	0.37	0.00	81.0
03MB11 R	117	38.5	0.08	0.03	0.04	39.3	0.28	0.40	22.6	0.13	101.4	0.99	0.00	0.00	0.00	1.51	0.01	0.01	0.49	0.00	75.6
03MB11 br	107	39.0	0.00	0.16	0.04	37.8	0.42	0.58	22.2	0.08	100.3	1.01	0.00	0.01	0.00	1.46	0.01	0.01	0.48	0.00	75.2
03MB11 gr	118	41.0	0.05	0.00	0.00	49.9	0.16	0.57	8.70	0.08	100.5	1.00	0.00	0.00	0.00	1.81	0.00	0.01	0.18	0.00	91.1
03MB11 br	119	37.8	0.16	0.07	0.07	25.9	0.43	0.88	33.2	0.11	98.6	1.05	0.00	0.00	0.00	1.08	0.01	0.02	0.77	0.00	58.2
03MB11 ws	121	39.3	0.06	0.01	0.00	44.5	0.14	0.64	15.8	0.11	100.6	0.99	0.00	0.00	0.00	1.67	0.00	0.01	0.33	0.00	83.3
03MB11 sp	123	40.0	0.03	0.00	0.01	44.8	0.20	0.61	15.1	0.09	100.8	1.00	0.00	0.00	0.00	1.67	0.01	0.01	0.32	0.00	84.1
03MB12 C	57	42.8	0.03	0.03	0.00	57.3	0.05	0.45	0.59	0.21	101.5	1.00	0.00	0.00	0.00	1.98	0.00	0.01	0.01	0.00	99.4
03MB12 C	58	42.5	0.03	0.04	0.00	57.0	0.08	0.21	0.65	0.32	100.8	0.99	0.00	0.00	0.00	1.98	0.00	0.00	0.01	0.01	99.4
03MB12 C	59	42.7	0.03	0.05	0.00	57.1	0.04	0.30	0.68	0.13	101.0	1.00	0.00	0.00	0.00	1.98	0.00	0.01	0.01	0.00	99.3
03MB12 C	60	42.4	0.01	0.01	0.00	57.2	0.06	0.20	0.61	0.32	100.9	0.99	0.00	0.00	0.00	1.99	0.00	0.00	0.01	0.01	99.4
03MB12 C	61	42.4	0.05	0.02	0.00	56.6	0.29	0.47	0.67	0.20	100.7	0.99	0.00	0.00	0.00	1.98	0.01	0.01	0.01	0.00	99.3
03MB12 R	62	42.0	0.00	0.03	0.00	56.6	0.10	0.41	0.60	0.21	99.9	0.99	0.00	0.00	0.00	1.99	0.00	0.01	0.01	0.00	99.4
03MB12 R	63	42.5	0.06	0.06	0.00	57.4	0.09	0.25	0.61	0.24	101.1	0.99	0.00	0.00	0.00	1.99	0.00	0.01	0.01	0.00	99.4
03MB12 R	64	42.8	0.07	0.03	0.00	57.4	0.06	0.29	0.65	0.13	101.4	0.99	0.00	0.00	0.00	1.99	0.00	0.01	0.01	0.00	99.4
03MB12 R	65	42.2	0.02	0.02	0.00	56.9	0.08	0.24	0.57	0.24	100.2	0.99	0.00	0.00	0.00	1.99	0.00	0.01	0.01	0.01	99.4
03MB12 R	66	42.8	0.02	0.02	0.01	57.1	0.10	0.40	0.64	0.20	101.3	1.00	0.00	0.00	0.00	1.98	0.00	0.01	0.01	0.00	99.4

(continued)

Table 1: Continued

Sample	<i>n</i>	Results in oxide wt %										Cations based on 4 oxygens									
		SiO <sub>2</sub>	TiO <sub>2</sub>	Al <sub>2</sub> O <sub>3</sub>	Cr <sub>2</sub> O <sub>3</sub>	MgO	CaO	MnO	FeO	NiO	Sum	Si	Ti	Al	Cr	Mg	Ca	Mn	Fe	Ni	Fo
03MB18 C	67	42.6	0.03	0.03	0.00	55.7	0.14	0.20	2.79	0.25	101.7	1.00	0.00	0.00	0.00	1.94	0.00	0.00	0.06	0.01	97.3
03MB18 C	68	42.5	0.00	0.08	0.00	56.1	0.06	0.28	0.88	0.17	100.0	1.00	0.00	0.00	0.00	1.97	0.00	0.01	0.02	0.00	99.1
03MB18 C	69	42.5	0.00	0.06	0.00	56.8	0.08	0.38	1.71	0.18	101.7	0.99	0.00	0.00	0.00	1.97	0.00	0.01	0.03	0.00	98.3
03MB18 C	70	42.7	0.00	0.05	0.01	55.8	0.09	0.40	1.74	0.21	101.0	1.00	0.00	0.00	0.00	1.95	0.00	0.01	0.03	0.00	98.3
03MB18 C	71	42.5	0.00	0.03	0.03	55.6	0.07	0.25	2.29	0.29	101.1	1.00	0.00	0.00	0.00	1.94	0.00	0.01	0.05	0.01	97.7
03MB18 R	73	42.5	0.08	0.14	0.00	57.0	0.10	0.29	1.06	0.13	101.3	0.99	0.00	0.00	0.00	1.98	0.00	0.01	0.02	0.00	99.0
03MB18 R	74	43.0	0.06	0.14	0.00	53.1	0.14	0.37	2.42	0.16	99.4	1.02	0.00	0.00	0.00	1.88	0.00	0.01	0.05	0.00	97.5
03MB18 R	75	42.6	0.05	0.05	0.00	57.0	0.07	0.44	1.18	0.11	101.6	0.99	0.00	0.00	0.00	1.98	0.00	0.01	0.02	0.00	98.9
03MB18 br	78	39.1	0.03	0.99	0.18	29.5	0.21	0.29	28.8	0.27	99.4	1.05	0.00	0.03	0.00	1.18	0.01	0.01	0.65	0.01	64.6
03MB19 C	125	40.2	0.01	0.05	0.04	47.2	0.15	0.13	12.4	0.24	100.4	0.99	0.00	0.00	0.00	1.74	0.00	0.00	0.26	0.01	87.1
03MB19 C	126	40.6	0.04	0.05	0.00	48.1	0.06	0.16	11.2	0.30	100.5	1.00	0.00	0.00	0.00	1.76	0.00	0.00	0.23	0.01	88.4
03MB19 C	127	40.2	0.01	0.04	0.02	47.0	0.23	0.24	12.7	0.27	100.7	0.99	0.00	0.00	0.00	1.73	0.01	0.01	0.26	0.01	86.8
03MB19 C	128	40.9	0.00	0.05	0.05	47.4	0.20	0.19	11.4	0.30	100.6	1.01	0.00	0.00	0.00	1.74	0.01	0.00	0.24	0.01	88.1
03MB19 C	129	40.1	0.00	0.03	0.00	46.6	0.25	0.26	13.1	0.15	100.6	1.00	0.00	0.00	0.00	1.72	0.01	0.01	0.27	0.00	86.3
03MB19 R	130	40.1	0.04	0.04	0.05	45.8	0.24	0.25	13.4	0.20	100.1	1.00	0.00	0.00	0.00	1.70	0.01	0.01	0.28	0.00	85.9
03MB19 R	131	40.3	0.00	0.04	0.00	48.4	0.08	0.38	9.87	0.13	99.2	1.00	0.00	0.00	0.00	1.78	0.00	0.01	0.20	0.00	89.7
03MB19 R	132	40.8	0.05	0.04	0.03	47.3	0.17	0.30	13.0	0.20	101.9	1.00	0.00	0.00	0.00	1.72	0.00	0.01	0.27	0.00	86.6
03MB19 R	133	39.8	0.04	0.04	0.02	45.1	0.12	0.28	15.0	0.14	100.6	1.00	0.00	0.00	0.00	1.68	0.00	0.01	0.31	0.00	84.3
03MB19 R	134	40.5	0.03	0.02	0.04	48.1	0.29	0.41	12.2	0.11	101.7	0.99	0.00	0.00	0.00	1.75	0.01	0.01	0.25	0.00	87.5
03MB19 W	135	41.0	0.00	0.02	0.04	49.5	0.21	0.14	9.73	0.31	101.0	1.00	0.00	0.00	0.00	1.79	0.01	0.00	0.20	0.01	90.1
03MB19 N	136	42.1	0.02	0.01	0.00	53.5	0.19	0.21	5.70	0.21	102.0	1.00	0.00	0.00	0.00	1.88	0.01	0.00	0.11	0.00	94.4

03MB29: oldest; 03MB19: youngest. C, core, R, rim, and other abbreviations reflect textures seen in Fig. 1: gr, granular; ba, band; br, bright; ws, wispy; sp, splotchy; W, western quadrant of grain; N, northern. *n*, analysis number.

1969). The measured  $\delta^{18}\text{O}$  values of the 03MB43 $\otimes$  forsterite are  $5.4 \pm 0.3\%$  ( $1\sigma$ ), within the uncertainty of mantle values, and therefore this sample is clearly not a carbonate-derived forsterite xenocryst. If the forsterites were assimilated xenocrysts, we would expect (1) a mix of forsterite and olivine within a single flow and (2) evidence of associated phase assimilation in the bulk-rock chemical signature or in the mineralogy. In the Papoose Canyon basalts, each flow has either forsteritic or normal olivine, with no mixing. Furthermore, we see no correlation between the whole-rock chemistry of a flow and the presence of forsterite in that flow (Fig. 4). In addition, the extremely low NiO concentrations found in serpentines and regenerated olivines are not seen in the Papoose Canyon basalts (Trommsdorff & Evans, 1974; Evans, 1977; Vance & Dungan, 1977; Nozaka, 2003; Blondes *et al.*, 2008).

### Subsolidus oxidation of magmatic phenocrysts in air

#### *Mineralogical, structural, and chemical evidence*

Multiple lines of evidence suggest an origin by high-temperature subsolidus oxidation. The symplectite

features and non-equilibrium embayed texture of the Papoose Canyon forsterite suggest post-crystallization alteration (Fig. 2a). The phases that typically form in subsolidus oxidation, symplectite laminae of olivine, pyroxene and hematite, are present in the Papoose Canyon forsterite (Johnston & Stout, 1984b). In the flows with normal olivine, magnetite is present in the rock, whereas the flows with forsterite contain only hematite as the iron oxide phase, both internal and external to the olivine. From this we know that the olivine experienced  $f\text{O}_2$  above the hematite–magnetite buffer. If  $\text{Fe}^{2+}$  is able to oxidize continuously, there is no maximum limit to forsterite content. Deer *et al.* (1992) showed that symplectite lamellae form by oxidation in specific crystallographical relationships with the host olivine. In the Papoose Canyon samples, the symplectite lamellae are parallel to the crosshairs at olivine extinction on an optical microscope, supporting a topotaxial relationship between the forsterite and the symplectite planes. EBSD results on the 03MB43 $\otimes$  forsterite show that the [100] direction of the olivine is parallel to the [0001] direction of hematite. This indicates that the hematite inherited the closest

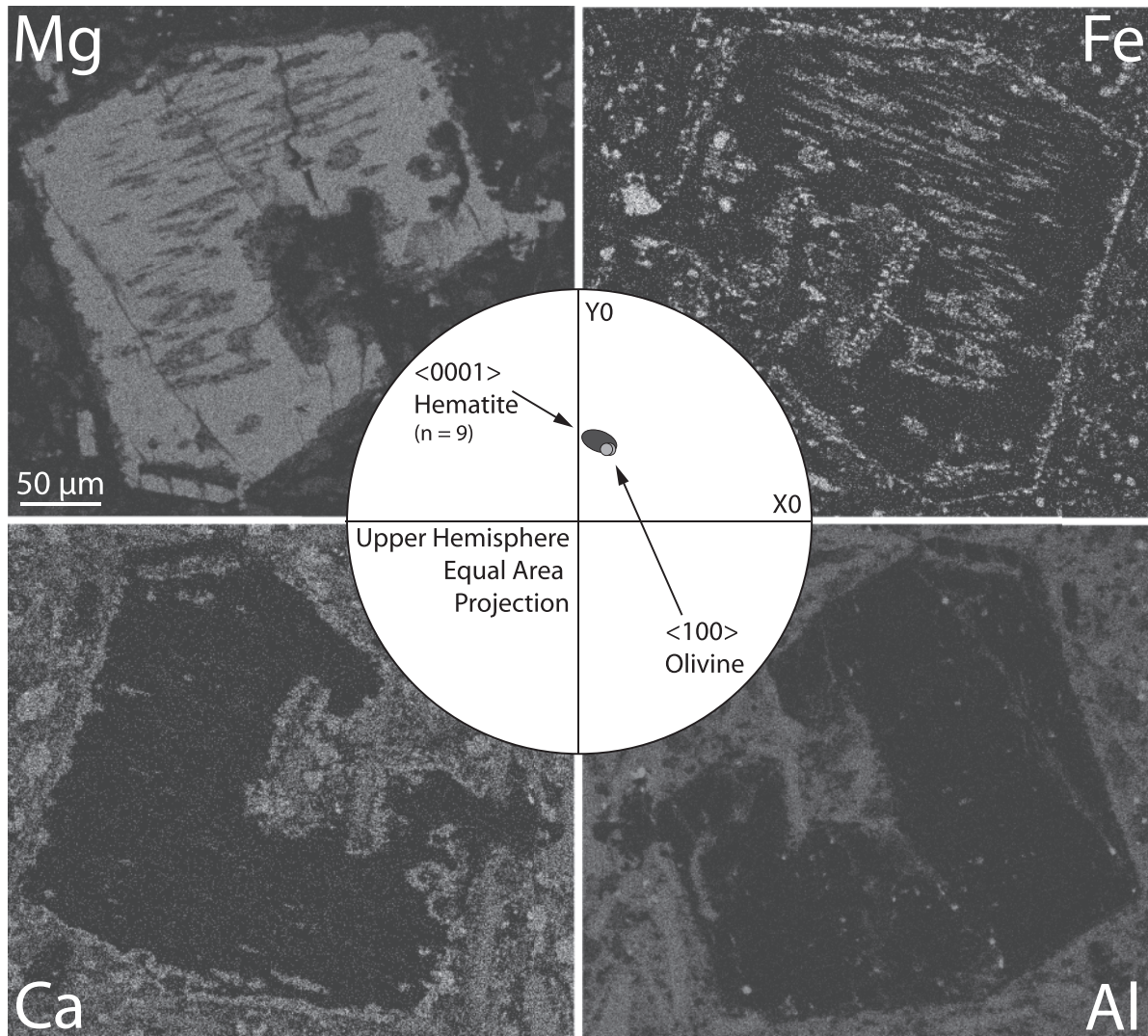


**Fig. 3.** Element maps of the 03MB43 $\otimes$  olivine grain. EMPA X-ray maps of Mg, Fe, Ca, and Al for the same olivine grain as in Fig. 2a. Brighter regions represent high concentrations of the listed element. The forsterite is best seen in the upper left figure with regions of high Mg. Hematite is best seen in the upper right image with regions of high Fe, both on the rim of the forsterite and in parallel planes within the grain. Clinopyroxene is best seen in the Ca figure on the lower left, and plagioclase in the Al figure on the lower right. Inset: EBSD orientation results for the 03MB43 $\otimes$  olivine and its hematite inclusions. X0 and Y0 are the thin section axes. The *a*-axis of the olivine is parallel to the *c*-axis of hematite so that closest packed planes of oxygen are aligned, demonstrating a topotaxial relationship between the two minerals.

packed oxygen planes of the olivine, a feature of oxidation (Moseley, 1984; Banfield *et al.*, 1990; Ashworth & Chambers, 2000) (Fig. 3).

We can calculate the composition of the original olivine host by integrating the size and composition of the present olivine along with all of its internal phases. First, we made a phase classification based on a backscattered electron (BSE) image of 03MB43 $\otimes$  (Fig. 1a), and calculated the modal per cent of olivine, hematite, clinopyroxene, and plagioclase. Because there were large dark (in BSE) cracks with light edges that spanned the entire grayscale range, we designated the cracks to be whatever phase they were crossing, which was dominantly olivine.

The composition of each phase was represented by the mean value of spot analyses from sample 03MB43 $\otimes$ , consisting of five spots from forsterite, three from hematite, three from clinopyroxene, and two from plagioclase (Table 2). Pyroxene is a minor phase, and most is clinopyroxene, so pyroxene was represented using the average clinopyroxene composition. This implies potential, but probably minor, overestimations of Ca and underestimations of Mg. The reintegration gives a composition of  $\text{Mg}_{1.5}\text{Fe}_{0.2}\text{Ca}_{0.1}\text{Si}_{1.0}\text{Al}_{0.05}\text{O}_4$ , which is an Fo<sub>86.3</sub> olivine. This composition is what we expect for typical basaltic olivine phenocrysts and is similar to normal phenocrystic olivine in other Papoose Canyon flows.

Table 2: Phases internal to 03MB43 olivine

Sample	<i>n</i>	Results in oxide wt %											Cations based on <i>n</i> oxygens												
		SiO <sub>2</sub>	TiO <sub>2</sub>	Al <sub>2</sub> O <sub>3</sub>	Cr <sub>2</sub> O <sub>3</sub>	MgO	CaO	MnO	FeO	NiO	K <sub>2</sub> O	Na <sub>2</sub> O	Sum	Si	Ti	Al	Cr	Mg	Ca	Mn	Fe	Ni	K	Na	O
Plag	180	53.4	0.00	27.6	0.00	0.00	11.1	0.00	1.38	0.00	0.25	4.87	98.6	2.5	0.0	1.5	0.0	0.5	0.0	0.0	0.0	0.0	0.0	0.4	8
Plag	181	56.1	0.00	26.7	0.00	0.00	9.28	0.01	1.28	0.00	0.39	5.45	99.2	2.5	0.0	1.4	0.0	0.5	0.0	0.0	0.0	0.0	0.0	0.5	8
Pyx	174	54.4	0.00	0.65	0.00	16.5	19.5	0.21	6.66	0.02	0.03	2.06	99.9	2.0	0.0	0.0	0.0	0.9	0.8	0.0	0.2	0.0	0.0	0.1	6
Pyx	175	52.7	0.07	0.84	0.02	15.9	19.1	0.23	7.84	0.02	0.02	2.15	98.9	2.0	0.0	0.0	0.0	0.9	0.8	0.0	0.2	0.0	0.0	0.2	6
Pyx	185	53.3	0.02	0.90	0.08	17.0	20.8	0.15	5.55	0.02	0.01	1.53	99.3	2.0	0.0	0.0	0.0	0.9	0.8	0.0	0.2	0.0	0.0	0.1	6
Hem	176	0.08	2.22	0.62	0.71	1.27	0.15	0.31	92.7	0.00	0.00	0.00	98.0	0.0	0.2	0.1	0.1	0.2	0.0	0.0	7.4	0.0	0.0	0.0	12
Hem	177	0.06	1.42	0.66	0.12	0.74	0.65	0.25	94.6	0.00	0.00	0.00	98.5	0.0	0.1	0.1	0.0	0.1	0.0	0.0	7.6	0.0	0.0	0.0	12
Hem	178	0.05	2.64	0.79	3.02	1.29	0.17	0.31	89.4	0.07	0.00	0.04	97.8	0.0	0.2	0.1	0.3	0.2	0.0	0.0	7.2	0.0	0.0	0.0	12

Plag, plagioclase; Pyx, pyroxene; Hem, hematite. *n*, number of analyses.

Table 3:  $\delta^{18}\text{O}$  results for the 03MB43 olivine grain

Sample	$\delta^{18}\text{O}$ (VSMOW)	$2\sigma$	$\delta^{18}\text{O}$ (raw)
MB43_OI-1	5.15	0.43	9.61
MB43_OI-2	5.19	0.43	9.65
MB43_OI-3	5.77	0.43	10.23
MB43_OI-5	5.59	0.43	10.05
Average	5.42	0.30	(1 $\sigma$ )

### Source of high $f\text{O}_2$

If the forsterite formed by a mechanism as simple as near-surface oxidation in the presence of atmospheric oxygen, we must address why forsterite is not more common in basaltic flows. The Cortés *et al.* (2006) study of Stromboli provides one of the closest analogues to the Big Pine Volcanic Field samples, although the Strombolian eruptive products appear to be less oxidized than the Big Pine basalts. Cortés *et al.* proposed that Fo<sub>97.4</sub> olivine formed by non-equilibrium degassing of fluid phases other than water owing to sudden decompression of the magma chamber. Sigurdsson & Brown (1970) suggested that Fo<sub>98.8</sub> olivine crystallized in melts oxidized by the dissociation of seawater. Haggerty & Baker (1967) provided experimental evidence for oxidation of Fo<sub>80</sub> olivine in air at atmospheric pressure ( $f\text{O}_2 = 10^{-0.68}$ ) from 24 to 100 h and 600 to 1000°C, and generated hematite and olivine that steadily increased the olivine Mg-number up to Fo<sub>99.9</sub>. These phases form symplectite planes crystallographically oriented within the olivine host and as reaction rims. Because we see clear textural evidence for subsolidus oxidation that is supported by models of hot oxidation in air,

we do not think it is necessary to invoke either water dissociation or non-equilibrium degassing.

Another possible mechanism to increase  $f\text{O}_2$  involves carbonates. Carbonate melting may have an effect on the oxidation state of the lavas, but only close to the xenolith–basalt interface. Wenzel *et al.* (2002) have suggested that the source of up to Fo<sub>98.7</sub> olivine in skarns is due to the melting of calcite, where it breaks down to form CaO and CO<sub>2</sub>. A nearly pure CO<sub>2</sub> fluid in a C–O–H system released from calcite can locally increase  $f\text{O}_2$  above the hematite–magnetite (HM) buffer, and crystallize forsteritic olivine adjacent to the entrained xenolith. Carbonate assimilation has multiple ancillary effects on the melt. According to experiments on basalt doped with calcite or dolomite, all of the carbonate is consumed, SiO<sub>2</sub> activity will decrease, CaO and substituting Sr will increase, olivine will cease crystallization and may be consumed, and calcic pyroxene will crystallize (Marziano *et al.*, 2007, 2008). This would be consistent with the elevated Ca and clinopyroxene rims in some of the forsterite grains (Figs 2 and 3, Table 1). However, although Fo<sub>94</sub> olivine is found in some natural volcanic samples that have assimilated carbonates (Marziano *et al.*, 2007), the forsterite content does not increase appreciably upon experimental calcite assimilation, but rather only with the input of Mg-bearing dolomite. Furthermore, we do not see any coincident increase in CaO or Sr within the whole-rocks containing the forsterite compared with the flows with normal olivine (Fig. 4). Therefore, we discount carbonate assimilation as a mechanism for increased  $f\text{O}_2$  in basaltic melts. Although high CO<sub>2</sub> may increase  $f\text{O}_2$  in the immediate vicinity of calcite xenoliths (Wenzel *et al.*, 2002), the necessary pure CO<sub>2</sub> fluid composition is unrealistic for entire basaltic lava flows. An increase in  $f\text{O}_2$  would occur only if CO<sub>2</sub> were to dissociate, but we see no mineralogical

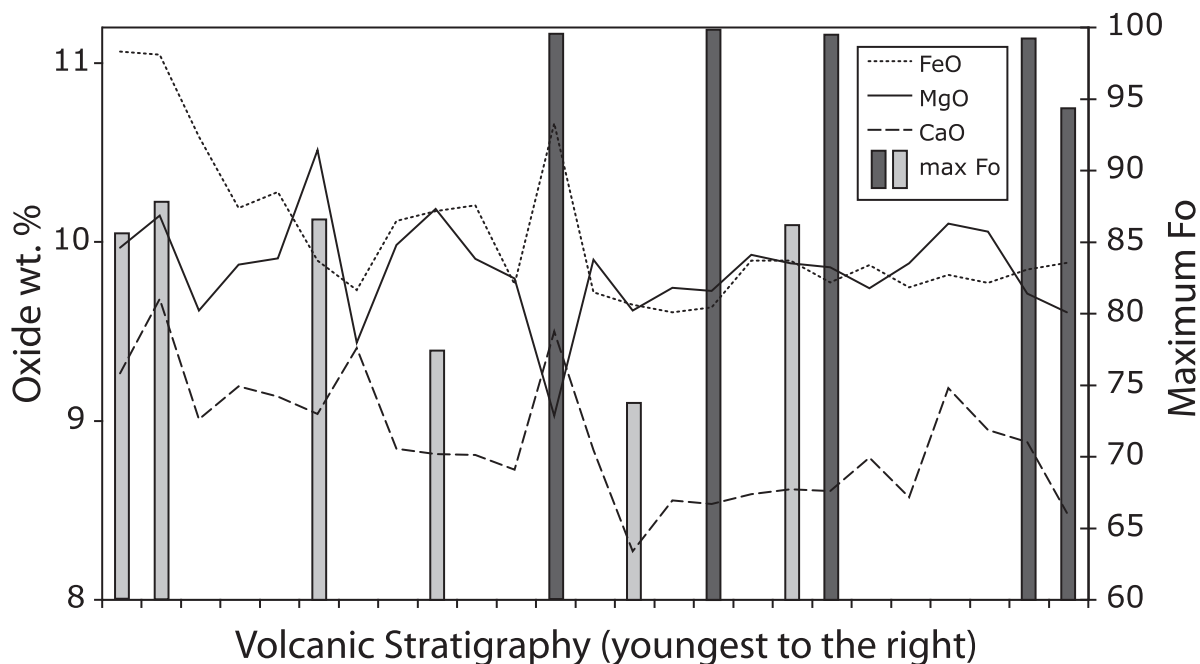


**Fig. 4.** Whole-rock and mineral Fo content as a function of eruption sequence. There is no correlation between whole-rock major element concentrations (Blondes *et al.*, 2008) and the flows that contain high-Fo olivine. The bimodal population of olivine is also evident, with the dark grey bars representing flows with only forsterite and the light grey bars representing flows with only normal olivine.

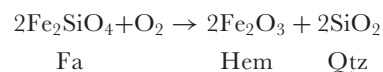
evidence for the reducing environment that this would require.

### Rarity of forsterite phenocrysts

If the forsterite did form by subsolidus oxidation in air, why is it uncommon? We have found only ~20 published natural olivine analyses with  $>F_{0.95}$ , out of perhaps of the order of tens of thousands of olivine analyses of magma phenocrysts and peridotitic samples. Of these, only a handful may be directly due to oxidation (Sigurdsson & Brown, 1970; Johnston & Stout, 1984a; Garcia *et al.*, 2000; Cortés *et al.*, 2006). However, if we consider the conditions that must be met for oxidation to proceed to forsteritic compositions, the Papoose Canyon single eruption sequence becomes an ideal location to find such forsterite. The basalt of this eruption is hot, primitive, and in some areas consists of a number of thin (<5 cm) stacked flows. The forsterite grains are not found within the underlying, thicker flows, but rather only in the later, thinner flows. A quick succession of thin, hot, vesicular flows, such as from quick lava spatter pulses, will allow the original olivine phenocrysts to cool much more slowly, while exposed to air, than those in the middle of a massive, minimally vesicular basalt flow (Fig. 5). Unlike most flows that cool between eruptions, the olivine (later forsterite) stayed hot with a continuous overburden of hot lava.

We can model the  $fO_2$  of the olivine to forsterite transition during slow cooling using coexisting forsterite,

pyroxene, and hematite, and assuming a range of appropriate temperatures. Experimental results of olivine oxidation in air at high temperatures show that for temperatures of 600–1130°C, hematite is the stable oxide phase (Haggerty & Baker, 1967; Gualtieri *et al.*, 2003). The remaining forsterite will react with product silica to form pyroxene, but the first reaction to hematite defines the relevant buffer. This reaction in the Fe–Si–O system defines the fayalite–hematite–quartz buffer (FHQ):



Using the free energies of formation at 1 bar and high temperatures (Robie & Hemingway, 1995), we calculate the  $fO_2$  vs  $T$  buffer relationship for the FHQ reaction (Fig. 5). Quartz and hematite, both pure solid phases, are assumed to have activities of one. Assuming ideal mixing, the activity of the fayalite component of the olivine solid solution is equal to its mole fraction ( $a_{\text{Fa}} = X_{\text{Fa}}$ ; Williams, 1972; Wood & Kleppa, 1981). Thus

$$\log_{10}(fO_2) = \left( \frac{\Delta G_{\text{rxn}}}{RT} \right) - 2 \log_{10}(X_{\text{Fa}}).$$

The FHQ buffers for hypothetical  $F_{0.90}$  ( $a_{\text{Fa}} = 0.10$ ),  $F_{0.95}$  ( $a_{\text{Fa}} = 0.05$ ), and  $F_{0.99}$  ( $a_{\text{Fa}} = 0.01$ ) olivine are shown in Fig. 5.

At 600–1130°C, the range of temperatures at which hematite is stable in olivine (Gualtieri *et al.*, 2003), the

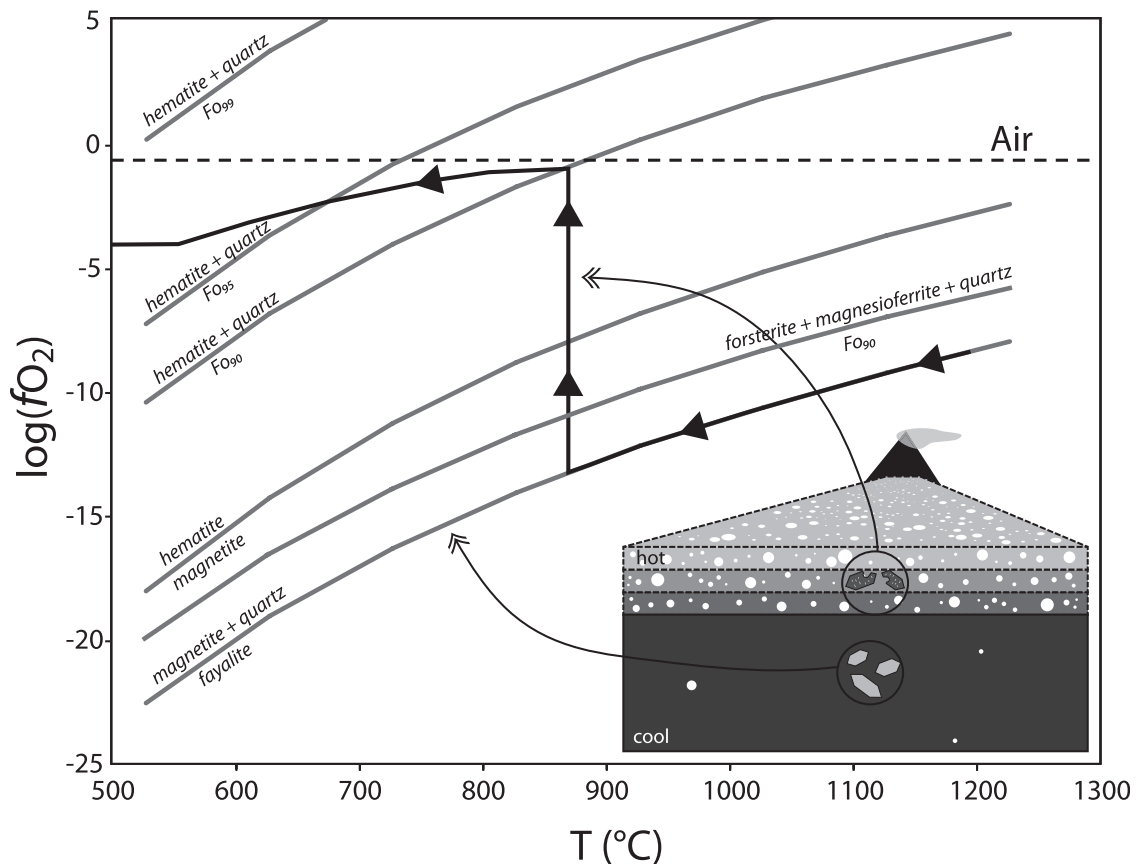


**Fig. 5.** The fayalite–hematite–quartz (FHQ) buffer, which is calculated for a range of forsterite contents in the olivine solid solution. Hematite–magnetite (HM), fayalite–magnetite–quartz (FMQ), and olivine–forsterite–magnesioferrite–quartz buffers are shown for reference. The black line represents a potential path for the forsteritic olivine in  $\log fO_2$  vs temperature space, as described in the text. The inset figure represents a series of stacked flow units from a monogenetic volcano. The thicker, massive basaltic unit at the bottom contains normal olivine phenocrysts, and the thin, hot, and vesicular flows at the top contain the forsterite grains. The dashed lines represent sustained interaction with air. The buffer including magnesioferrite represents low-temperature oxidation in olivine (Khisina *et al.*, 1995).

corresponding range of  $fO_2$  on the FHQ buffer ( $10^{-8}$ – $10^3$ ) encompasses the  $fO_2$  of air ( $10^{-0.68}$ ) (Fig. 5). A normal olivine phenocryst typically records the oxidation conditions of the magma, usually between the FMQ and NNO buffers. Upon eruption, olivine within the dense interior of a single thick lava flow will not significantly interact with air and will cool along the QFM buffer, with no formation of hematite or forsterite. These interior olivines, however, may form lower temperature oxidation products of olivine such as magnesioferrite (Khisina *et al.*, 1995), which is present in some of the Big Pine samples (Figs 2 and 5). In contrast, for the highly vesicular, thin lava spatter units, the temperature will remain high with repeated eruptions while abundant air is trapped in the vesicles. The oxidized olivine is no longer buffered by magnetite and reaches the FHQ<sub>Fo90</sub> buffer near the  $fO_2$  of air. The olivine will then slowly cool along a series of FHQ<sub>Fo90</sub>–FHQ<sub>Fo99</sub> buffers as the Mg-number of the olivine increases (Fig. 5). At  $\sim 600^\circ\text{C}$ , the reaction will cease.

Following this model, we expect similar near end-member forsterite in other rapidly emplaced basalt flows or at the upper boundaries of thicker flows where they have been quickly covered by subsequent ones. They are only rarely found now because the normal methods of sample collection usually require a ‘fresh’ sample from the middle of a flow, and geologists tend to avoid altered hand samples and olivine for analysis. Because these particular flows are so thin, we were forced to sample only regions that were highly oxidized, and predict that near end-member forsterite is actually much more common than previously recognized.

## CONCLUSIONS

Results of oxygen isotope, EBSD, electron microprobe, petrographic and mineralogical analysis show that  $>Fo_{90}$  olivine formed during subsolidus continuous oxidation from air trapped in repeated hot lava flows. This interpretation

is consistent with theoretical and crystallographic evidence of pyroxene–Fe-oxides symplectite formation from oxidation. Near-pure forsterite in basaltic rocks previously may have appeared rare for the very fact that geologists tend to avoid highly altered flow boundaries or altered olivines when looking for fresh samples to analyze. The section of the monogenetic eruption in which these forsterite grains are found consists of many thin, vesicular flows erupted over a short ( $10^0$ – $10^2$  years) time-scale. This may be the ideal type of environment to locate pure forsterite, because the magmas were primitive with high-Mg phenocrysts to start with, and subsequent hot flows were erupted in rapid succession, keeping previous thin flows hot while exposed to air. If the conclusions of this study are correct, we would expect to find many such forsterite grains in any location where hot, primitive basalts erupt in thin flows over very short periods of time.

## ACKNOWLEDGEMENTS

We appreciate constructive reviews from Michael Dungan, Eric Christiansen, and Joaquin Cortés, and helpful discussion from Rosalind Helz. John Valley assisted in SIMS analysis and reviewed an early version of this paper.

## FUNDING

F.Z.P. made SIMS analyses while supported as a post-doctoral fellow at UW-Madison by NSF (EAR0440343) and DoE (93ER14389). Wisc-SIMS is partly supported by NSF (EAR03-19230, EAR05-16725, EAR07-44079).

## SUPPLEMENTARY DATA

Supplementary data for this paper are available at *Journal of Petrology* online.

## REFERENCES

- Ando, J., Shibata, Y., Oka Jima, Y., Kanagawa, K., Furusho, M. & Tomioka, N. (2001). Striped iron zoning of olivine induced by dislocation creep in deformed peridotites. *Nature* **414**, 893–895.
- Ashworth, J. R. & Chambers, A. D. (2000). Symplectitic reaction in olivine and the controls of intergrowth spacing in symplectites. *Journal of Petrology* **41**, 285–304.
- Banfield, J. F., Veblen, D. R. & Jones, B. F. (1990). Transmission electron microscopy of subsolidus oxidation and weathering of olivine. *Contributions to Mineralogy and Petrology* **106**, 110–123.
- Beard, B. L. & Glazner, A. F. (1995). Trace element and Sr and Nd isotopic composition of mantle xenoliths from the Big Pine volcanic field, California. *Journal of Geophysical Research* **100**, 4169–4179.
- Blondes, M. S., Reiners, P. W., Edwards, B. R. & Biscontini, A. (2007). Dating young basalt eruptions by (U–Th)/He on xenolithic zircons. *Geology* **35**, 17–20.
- Blondes, M. S., Reiners, P. W., Duca, M. N., Singer, B. S. & Chesley, J. (2008). Temporal–compositional trends over short and long time-scales in basalts of the Big Pine Volcanic Field, California. *Earth and Planetary Science Letters* **269**, 140–154.
- Bowen, N. L. & Schairer, J. F. (1935). The system MgO–FeO–SiO<sub>2</sub>. *American Journal of Science* **29**, 151–217.
- Boyd, F. R. & Nixon, P. H. (1978). Ultramafic nodules from the Kimberley pipes, South Africa. *Geochimica et Cosmochimica Acta* **42**, 1367–1382.
- Champness, P. E. (1970). Nucleation and growth of iron oxides in olivines, (Mg,Fe)<sub>2</sub>SiO<sub>4</sub>. *Mineralogical Magazine* **37**, 790–800.
- Cook, S. J. & Bowman, J. R. (2000). Mineralogical evidence for fluid–rock interaction accompanying prograde contact metamorphism of siliceous dolomites: Alta Stock Aureole, Utah, USA. *Journal of Petrology* **41**(6), 739–757.
- Cortés, J. A., Wilson, M., Condliffe, E. & Francalanci, L. (2006). The occurrence of forsterite and highly oxidizing conditions in basaltic lavas from Stromboli volcano, Italy. *Journal of Petrology* **47**, 1345–1373.
- Deer, W. A., Howie, R. A. & Zussman, J. (1992). *An Introduction to the Rock-forming Minerals*, 2nd edn. Harlow: Longman.
- Ducea, M. N. & Saleeby, J. B. (1998). A case for delamination of the deep batholithic crust beneath the Sierra Nevada, California. *International Geological Review* **40**, 78–93.
- Eiler, J. M. (2001). Oxygen isotope variations of basaltic lavas and upper mantle rocks. In: Valley, J. W. & Cole, D. (eds) *Stable Isotope Geochemistry*. Mineralogical Society of America and Geochemical Society, *Reviews of Mineralogy and Geochemistry* **43**, 319–364.
- Eiler, J. M., Farley, K. A., Valley, J. W., Hauri, E., Graig, H., Hart, S. R. & Stolper, E. M. (1997a). Oxygen isotope variations in ocean island basalt phenocrysts. *Geochimica et Cosmochimica Acta* **61**, 2281–2293.
- Eiler, J. M., Graham, C. M. & Valley, J. W. (1997b). SIMS analysis of oxygen isotopes; matrix effects in complex minerals and glasses. *Chemical Geology* **138**, 221–244.
- Evans, B. W. (1977). Metamorphism of Alpine peridotite and serpentinite. *Annual Review of Earth and Planetary Sciences* **5**, 397–447.
- Ferry, J. M. (1994). Role of fluid flow in the contact metamorphism of siliceous dolomitic limestones. *American Mineralogist* **79**, 719–736.
- Garcia, M. O., Pietruszka, A. J., Rhodes, J. M. & Swanson, K. (2000). Magmatic processes during the prolonged Pu‘u O‘o eruption of Kilauea volcano, Hawaii. *Journal of Petrology* **41**, 967–990.
- Goode, A. D. T. (1974). Oxidation of natural olivines. *Nature* **248**, 500–501.
- Gualtieri, A. F., Gemmi, M. & Dapiaggi, M. (2003). Phase transformations and reaction kinetics during the temperature-induced oxidation of natural olivine. *American Mineralogist* **88**, 1560–1574.
- Haggerty, S. E. & Baker, I. (1967). The alteration of olivine in basaltic and associated lavas. Part I: High temperature alteration. *Contributions to Mineralogy and Petrology* **16**, 233–257.
- Johnston, A. D. & Stout, J. H. (1984a). A highly oxidized ferrian salite-, kenedyite-, forsterite-, and rhonite-bearing alkali gabbro from Kauai, Hawaii and its mantle xenoliths. *American Mineralogist* **69**, 57–68.
- Johnston, A. D. & Stout, J. H. (1984b). Development of orthopyroxene–Fe/Mg ferrite symplectites by continuous olivine oxidation. *Contributions to Mineralogy and Petrology* **88**, 196–202.
- Karato, S. (1987). Scanning electron microscope observation of dislocations in olivine. *Physics and Chemistry of Minerals* **14**, 245–248.
- Khisina, N. R., Khramov, D. A., Kolosov, M. V., Kleschev, A. A. & Taylor, L. A. (1995). Formation of ferriolivine and magnesioferrite from Mg–Fe–olivine: Reactions and kinetics of oxidation. *Physics and Chemistry of Minerals* **22**, 241–250.
- Kita, N. T., Ushikubo, T., Fu, B. & Valley, J. W. (2009). High precision SIMS oxygen isotope analyses and the effect of sample topography. *Chemical Geology* **264**, 43–57.

- Kohlstedt, D. L. & Vander Sande, J. B. (1975). An electron microscopy study of naturally occurring oxidation produced precipitates in iron-bearing olivines. *Contributions to Mineralogy and Petrology* **53**, 13–24.
- Lee, C. A., Rudnick, R. L. & Brimhall, G. H., Jr (2001). Deep lithospheric dynamics beneath the Sierra Nevada during the Mesozoic and Cenozoic as inferred from the xenolith petrology. *Geochemistry, Geophysics, Geosystems* **2**, doi:10.1029/2001GC000152.
- Marziano, G. I., Gaillard, F. & Pichavant, M. (2007). Limestone assimilation and the origin of CO<sub>2</sub> emissions at the Alban Hills (Central Italy): Constraints from experimental petrology. *Journal of Volcanology and Geothermal Research* **166**, 91–105.
- Marziano, G. I., Gaillard, F. & Pichavant, M. (2008). Limestone assimilation by basaltic magmas: an experimental re-assessment and application to Italian volcanoes. *Contributions to Mineralogy and Petrology* **155**, 719–738.
- Menzies, M. A., Leeman, W. P. & Hawkesworth, C. J. (1983). Isotope geochemistry of Cenozoic volcanic rocks reveals mantle heterogeneity below western USA. *Nature* **303**, 205–209.
- Moseley, D. (1984). Symplectic exsolution in olivine. *American Mineralogist* **69**, 139–153.
- Nitsan, U. (1974). Stability field of olivine with respect to oxidation and reduction. *Journal of Geophysical Research* **79**, 706–711.
- Nozaka, T. (2003). Compositional heterogeneity of olivine in thermally metamorphosed serpentinite from Southwest Japan. *American Mineralogist* **88**, 1377–1384.
- Owens, B. E. (2000). High-temperature contact metamorphism of calc-silicate xenoliths in the Kiglapait Intrusion, Labrador. *American Mineralogist* **85**, 1595–1605.
- Page, F. Z., Kita, N. T. & Valley, J. W. (2010). Ion microprobe analysis of oxygen isotopes in garnets of complex chemistry. *Chemical Geology* **207**, 9–19.
- Petaev, M. I. & Brearley, A. J. (1994). Exsolution in ferromagnesian olivine of the Divnoe Meteorite. *Science* **266**, 1545–1547.
- Prior, D. J., Boyle, A. P., Brenker, F., Cheadle, M. C., Day, A., Lopez, G., Peruzzi, L., Potts, G., Reddy, S., Spiess, R., Timms, N. E., Trimby, P., Wheeler, J. & Zetterstrom, L. (1999). The application of electron backscatter diffraction and orientation contrast imaging in the SEM to textural problems in rocks. *American Mineralogist* **84**, 1741–1759.
- Putnis, A. (1979). Electron petrography of high-temperature oxidation in olivine from the Rhum Layered Intrusion. *Mineralogical Magazine* **43**, 293–296.
- Robie, R. A. & Hemingway, B. S. (1995). *Thermodynamic properties of minerals and related substances at 298-15 K and 1 bar (10<sup>5</sup> pascals) pressure and at higher temperatures*. US Geological Survey Bulletin **2131**, 461.
- Roeder, P. L. & Emslie, R. F. (1970). Olivine–liquid equilibrium. *Contributions to Mineralogy and Petrology* **29**, 275–289.
- Saleeby, J. B. (1982). Polygenetic ophiolite belt of the California Sierra Nevada: Geochronological and tectonostratigraphic development. *Journal of Geophysical Research* **87**, 1803–1824.
- Shannon, R. D. & Rossi, R. C. (1964). Definition of topotaxy. *Nature* **202**, 1000–1001.
- Shieh, Y. N. & Taylor, H. P., Jr (1969). Oxygen and carbon isotope studies of contact metamorphism of carbonate rocks. *Journal of Petrology* **10**, 307–331.
- Sigurdsson, H. & Brown, G. M. (1970). An unusual enstatite–forsterite basalt from Kolbeinsey Island, north of Iceland. *Journal of Petrology* **11**, 205–220.
- Sobolev, N. V., Bartoshinskiy, Z. V., Yefimova, E. S., Lavrent'ev, Yu. G. & Pospelova, L. N. (1970). Olivine–garnet–chrome–diopside assemblage from Yakutian diamond. *Doklady Academy of Sciences of the USSR, Earth Sciences Section* **192**, 134–137.
- Sobolev, A. V., Hofmann, A. W., Kuzmin, D. V., Yaxley, G. M., Arndt, N. T., Chung, S. L., Danyushevsky, L. V., Elliott, T., Frey, F. A., Garcia, M. O., Gurenko, A. A., Kamenetsky, V. S., Kerr, A. C., Krivolutsкая, N. A., Matvienkov, V. V., Nikogosian, I. K., Rocholl, A., Sigurdsson, I. A., Sushchevskaya, N. M. & Teklay, M. (2007). The amount of recycled crust in sources of mantle-derived melts. *Science* **316**, 412–417.
- Trommsdorff, V. & Evans, B. W. (1974). Alpine metamorphism of peridotitic rocks. *Schweizerische Mineralogische und Petrographische Mitteilungen* **54**, 333–352.
- Trommsdorff, V. & Evans, B. W. (1977). Antigorite–ophicarbonates: contact metamorphism in Valmalenco, Italy. *Contributions to Mineralogy and Petrology* **62**, 301–312.
- Valley, J. W. (1986). Stable isotope geochemistry of metamorphic rocks. In: Valley, J. W., Taylor, H. P., Jr & O'Neill, J. R. (eds) *Stable Isotopes in High Temperature Geological Processes*. Mineralogical Society of America, *Reviews in Mineralogy and Geochemistry* **16**, 445–489.
- Vance, J. A. & Dungan, M. A. (1977). Formation of peridotites by deserpentinization in the Darrington and Sultan areas, Cascade Mountains, Washington. *Geological Society of America Bulletin* **88**, 1497–1508.
- Wenzel, T., Baumgartner, L. P., Brugmann, G. E., Konnikov, E. G. & Kislov, E. V. (2002). Partial melting and assimilation of dolomitic xenoliths by mafic magma: the Ioko-Dovyren intrusion (North Baikal region, Russia). *Journal of Petrology* **43**, 2049–2074.
- Williams, R. J. (1972). Activity–composition relations in the fayalite–forsterite solid solution between 900° and 1300°C at low pressures. *Earth and Planetary Science Letters* **15**, 296–300.
- Wood, B. G. & Kleppa, O. J. (1981). Thermochemistry of forsterite–fayalite olivine solutions. *Geochimica et Cosmochimica Acta* **45**, 529–534.
- Zandt, G., Gilbert, H., Owens, T. J., Duca, M. N., Saleeby, J. B. & Jones, C. H. (2004). Active foundering of a continental arc root beneath the southern Sierra Nevada in California. *Nature* **431**, 41–46.